Available online at www.sciencedirect.com

ScienceDirect

Geochimica et Cosmochimica Acta xxx (2021) xxx–xxx

Geochimica et Cosmochimica Acta

www.elsevier.com/locate/gca

Thallium sorption by soil manganese oxides: Insights from synchrotron X-ray micro-analyses on a naturally thallium-rich soil

Francesco Femi Marafatto [a,c,*], Rainer Dähn [a], Daniel Grolimund [b], Jörg Göttlicher [d], Andreas Voegelin [c,*]

[a] *Paul Scherrer Institute, Laboratory of Waste Management, Forschungstrasse 111, Villigen PSI, CH-5232, Switzerland*
[b] *Paul Scherrer Institute, Swiss Light Source, microXAS beamline, Forschungstrasse 111, Villigen PSI, CH-5232, Switzerland*
[c] *Eawag, Department of Water Resources and Drinking Water, Ueberlandstrasse 133, Dübendorf, CH-8600, Switzerland*
[d] *Karlsruhe Institute of Technology, Institute for Photon Science and Synchrotron Radiation, KIT Campus North, Hermann-von-Helmholtz-Platz 1, Eggenstein-Leopoldshafen, D-76344, Germany*

Received 25 November 2020; accepted in revised form 8 March 2021; available online xxxx

Abstract

Thallium (Tl) is a highly toxic trace metal. It occurs mostly as soluble monovalent Tl(I) and less frequently as poorly soluble trivalent Tl(III). Laboratory studies have shown that vacancy-containing hexagonal birnessites can sorb Tl with a very high affinity via a mechanism that involves the oxidation of Tl(I) to Tl(III) and strong complexation of Tl(III), whereas other manganese (Mn) oxides bind Tl(I) non-oxidatively and with lower sorption affinity. Information on the mode of Tl uptake by natural Mn oxides in soils, on the other hand, is still limited. In this study, we characterized the association of Tl with Mn oxides and Tl (redox) speciation in a naturally Tl-rich soil using micro-focused synchrotron X-ray absorption near edge structure (XANES) spectroscopy and X-ray fluorescence (XRF) chemical imaging. The results show that most soil Tl was Tl(I) associated with micaceous clay minerals in the soil matrix. High levels of Tl in soil Mn concretions, on the other hand, were mostly identified as Tl(III), suggesting that oxidative Tl uptake by vacancy-containing hexagonal birnessite was the main process of Tl accumulation in soil Mn concretions. The spectroscopic results in combination with chemical extractions and published sorption isotherms for Tl on synthetic Mn oxides suggest that the formation and transformation of natural Mn oxides in soils and sorption competition of Tl with major and trace metal cations determine the extent and mode of Tl uptake by soil Mn oxides. Methodologically, this study compares classical micro-XRF element mapping combined with point XANES analyses for spatially-resolved element speciation with high-resolution chemical imaging of entire sample areas, which is of great interest for the geochemical community in light of diffraction-limited storage ring upgrades to many synchrotron lightsources.

Keywords: Thallium geochemistry; Soil; Manganese oxides; Synchrotron X-ray fluorescence microspectroscopy; Chemical imaging; Redox mapping

1. INTRODUCTION

Thallium is a highly toxic trace metal classified as a priority pollutant by the US environmental protection agency. The concentrations of Tl in soils are usually below 1 mg/kg,

* Corresponding authors.
E-mail addresses: francesco.marafatto@psi.ch (F.F. Marafatto), andreas.voegelin@eawag.ch (A. Voegelin).

https://doi.org/10.1016/j.gca.2021.03.011
0016-7037/

but exceptionally high concentrations up to several 1000 mg/kg may be found where soils develop on mineralized parent rock (Peter and Viraraghavan, 2005; Voegelin et al., 2015). Anthropogenic Tl contamination of soils results from cement production, metal mining and smelting, coal mining and burning, sulfuric acid production and other industrial activities (Vanek et al., 2010).

In the environment, Tl mostly occurs as monovalent Tl (I) and, to a lesser extent, as Tl(III). The Tl^+ cation has a similar ionic radius and a similar (low) hydration energy as K^+. Monovalent Tl(I) therefore reacts in analogy to K, can substitute K in minerals such as K-feldspar, mica or clay minerals, and is also relatively mobile and bioavailable in soils. The Tl^{3+} cation is strongly hydrolyzing and poorly soluble, Tl(III) therefore mainly occurs in avicennite (Tl_2O_3) or as a sorbed cation on certain Mn oxides (Cruz-Hernandez et al., 2019; Peacock and Moon, 2012; Voegelin et al., 2015; Wick et al., 2019). In soils, the sorption of Tl onto micaceous clay minerals and onto Mn oxides is assumed to control the solubility and thereby the mobility and bioavailability of Tl (Belzile and Chen, 2017; Jacobson et al., 2005; Vaněk et al., 2009; Voegelin et al., 2015; Wick et al., 2020). Therefore, knowing the speciation of Tl in soils is essential for the assessment of risks arising from Tl in contaminated soils.

Manganese oxides are known to affect the speciation and sequestration of a wide range of trace metals in soils and other environments (Fuller and Harvey, 2000; Manceau et al., 2007; Post, 1999), and Mn oxides have also been inferred to effectively sorb Tl in soils (Jacobson et al., 2005; Vanek et al., 2011). Using X-ray microspectroscopy, Tl has been shown to accumulate in Mn oxides in marine ferromanganese nodules (Peacock and Moon, 2012) and in Mn concretions in a contaminated soil (Voegelin et al., 2015). The mode of Tl sorption onto Mn oxides depends on their structure (Bidoglio et al., 1993; Cruz-Hernandez et al., 2019; Peacock and Moon, 2012; Wick et al., 2019). Hexagonal birnessites with uncapped vacancies in their octahedral sheets can oxidize Tl(I) and bind the Tl(III) with extremely high affinity (Peacock and Moon, 2012; Wick et al., 2019). Birnessite with or without blocked vacancies and todorokite strongly sorb Tl(I) as a hydrated cation in their interlayers or tunnels. In cryptomelane, dehydrated Tl^+ exchanges structural K^+ (Gołębiowska et al., 2021; Wick et al., 2019). In combination with sorption data, these findings suggest that the mode and strength of Tl binding onto Mn oxides in natural samples depends on the type of Mn oxide and on Tl loading (Wick et al., 2019).

In soils, Mn oxides often occur in concretions that form within and around soil mineral aggregates as a result of varying redox conditions, i.e., reductive mobilization of Mn^{2+} in temporarily waterlogged soil followed by localized microbial or autocatalytic Mn oxidation upon reaeration (Sposito, 2008; Tebo et al., 2007). Freshly-formed biogenic Mn oxides have been described as vacancy-rich hexagonal birnessite (Bargar et al., 2009; Tebo et al., 2004; Villalobos et al., 2005; Webb et al., 2005). The mineralogy of a soil Mn concretion in a clayey paddy soil was found to consist of a mixture of turbostratic hexagonal birnessite and lithioporite (Manceau et al., 2007). The accumulation of high levels of Tl in marine ferromanganese nodules has been attributed to the oxidative scavenging of Tl(III) by hexagonal birnessite from seawater, based on bulk X-ray absorption spectroscopy (XAS) analyses on Tl-sorbed Mn oxides and spatially resolved X-ray fluorescence spectrometry (XRF) and XAS on a Tl-rich ferromanganese nodule (Peacock and Moon, 2012). Also in a spectroscopic study on naturally Tl-rich soils from Erzmatt (Switzerland), elevated levels of Tl in a soil Mn concretion were shown to correspond to Tl(III) sorbed onto hexagonal birnessite (Voegelin et al., 2015). Recent results on the sorption and speciation of Tl in soils from the Erzmatt indicated that the Tl loading of soil Mn oxides was lower than observed for oxidative Tl(III) sorption onto hexagonal birnessite in laboratory sorption experiments (Wick et al., 2020), prompting for further research on the extent and mode of Tl uptake by soil Mn oxides. Owing to their ability to accumulate high amounts of Tl and their susceptibility to reductive dissolution, Mn oxides may critically impact on the retention and dynamics of Tl in contaminated soils (Vaněk et al., 2020). To gain further insights into the relevance and mode of Tl sorption onto soil Mn oxides, and into the transferability of results from laboratory sorption studies to soils, it is essential to get direct and spatially resolved information on the extent and mode of Tl association with Mn concretions in soils (Wick et al., 2020).

Spatially-resolved information on the speciation of trace elements in heterogeneous soil samples is classically obtained at synchrotron light sources by collecting X-ray fluorescence (XRF) element distribution maps on thin-sections using a micro-focused X-ray beam, followed by the analysis of the speciation of a selected element on discrete points by X-ray absorption spectroscopy (XAS) (Lombi and Susini, 2009; Manceau et al., 2002; Manceau et al., 2004). More recently, with advances in X-ray optics, detectors, electronics and computational power, it became possible to rapidly acquire high-resolution XRF maps where a full XRF spectrum is recorded for each pixel (Baruchel et al., 2008; De Samber et al., 2008). Taking advantage of this possibility, spatially resolved speciation information can now be obtained over entire sample areas by chemical imaging, i.e., by fast XRF mapping at multiple incident photon energies across the absorption edge of the target element (Grolimund et al., 2004; Lombi and Susini, 2009; Marcus, 2010). Because chemical imaging at selected energies allows to minimize the cumulative counting time per point, chemical information may also be accessible in cases where longer point XAS analyses are hampered by the radiation sensitivity of the sample matrix or the probed element (Gonçalves Ferreira et al., 2013; Teng and Moffat, 2000). Both Tl and Mn occur in multiple oxidation states and are radiation-sensitive elements (Manceau et al., 2012; Nielsen et al., 2013; Peacock and Moon, 2012). Therefore, the spatially resolved characterization of the speciation of Tl in soil Mn concretions represents a methodologically challenging task (Grabolle et al., 2006; Kirkbright et al., 1972).

In this study, we characterized the micrometer-scale association of Tl with soil Mn concretions in a naturally Tl-rich soil using synchrotron-based hard X-ray absorption

Please cite this article in press as: Marafatto F. F., et al. Thallium sorption by soil manganese oxides: Insights from synchrotron X-ray micro-analyses on a naturally thallium-rich soil. *Geochim. Cosmochim. Acta* (2021), https://doi.org/10.1016/j.gca.2021.03.011

spectroscopy and X-ray fluorescence analysis (chemical imaging) to gain new insights into the relevance and mechanism(s) of Tl sorption by soil Mn oxides. Specifically, we tested for variations in the redox speciation of Tl between soil Mn oxides and whether such variations could be linked to variations in the Tl loading of the Mn oxides. We used classical μ-XRF element distribution mapping together with point XANES analyses with 60 μm × 30 μm spatial resolution for more detailed localized information on Tl speciation as well as chemical imaging over an entire sample area with 5 μm spatial resolution for information on the link between the association of Tl with Mn oxides and Tl redox speciation. This combined approach offered more representative insights and also allowed us to compare advantages and disadvantages of the two analytical approaches.

2. MATERIALS AND METHODS

2.1. Sample selection and preparation

The soil material for this study was collected on the Erzmatt site in the Swiss Jura Mountains during a sampling campaign in 2013, at a depth of 38 cm in profile P1. The sampling site and the profile P1 have been described in detail previously (Voegelin et al., 2015). Bulk soil material was air-dried at 40 °C, ball-milled and stored in a plastic container in the dark. For the preparation of thin sections, an undisturbed block of soil was collected in an aluminum box ($4 \times 4 \times 3$ cm^3) with perforated walls. In the laboratory, the soil in the box was freeze dried, stored in the dark at room temperature and then impregnated before the synchrotron measurements (in 2017/2018) using 2-component epoxy resin (Araldite 2020). From the embedded blocks, polished thin sections with a thickness of ~30 μm were prepared on 1×1 cm^2 Si wafers that had first been thinned down to 250 μm thickness (Geoprep, Switzerland), to ensure good thermal contact (for measurements in a cryostat).

A total of 6 thin sections were prepared. Element distributions in the sections were pre-screened at a spatial resolution of ~20 μm using a laboratory μ-XRF instrument (M4 Tornado, Bruker Nano GmbH) equipped with an Ag X-ray tube for sample excitation, polycapillary X-ray optics for beam focusing, and two Si drift detectors for fluorescence detection. Based on these results, the most interesting section for synchrotron-based analyses was selected.

2.2. Chemical soil analyses

For chemical laboratory analyses, air-dried (40 °C) and powdered bulk soil material was used that had been sampled from the same depth as the undisturbed soil used for the preparation of thin sections. Total element contents were quantified by X-ray fluorescence spectrometry (Xepos+, SPECTRO Analytical Instruments GmbH, Germany). A 10 mM $CaCl_2$ extract (1 g of soil in 10 mL of 10 mM $CaCl_2$; 2 h reaction time) was performed to measure soil pH and to analyze dissolved Tl by inductively coupled plasma mass spectrometry (ICP-MS) as a proxy for Tl in the soil porewater (Houba et al., 2000). A sequential extraction was performed that consisted of two steps: (i) 3-fold extraction with 1 M NH_4-acetate at pH 6.8 to extract exchangeable Tl(I) (1 g of soil, 3 times 30 mL of solution, 30 min reaction time). (ii) 3-fold extraction with 0.1 M hydroxylamine hydrochloride ($NH_2OH{\cdot}HCl$) / 1 M NH_4-acetate at pH 6.1 to reductively extract Mn and associated Tl from Mn oxides (3 times 30 mL of solution, 30 min reaction time). For further methodological details, see Wick et al. (2020). The extracts were filtered, acidified and diluted for the analysis of extracted Mn and Tl by ICP-MS.

2.3. Synchrotron measurements at the SUL-X beamline at KARA

The SUL-X beamline at the Karlsruhe Research Accelerator (KARA) at the Karlsruhe Institute of Technology (KIT, Germany) is a wiggler beamline equipped with a fixed-exit double crystal monochromator (Si 111) and with a combination of slits and Kirkpatrick-Baez mirrors for beam focusing. The monochromator energy was calibrated to 12,658 eV at the first maximum of the first derivative of the K-edge of grey Se(0). The section was analyzed with a beam size of 60×30 μm^2 at room temperature. Data was collected in fluorescence mode using an IC-Plus type ion chamber from Oxford Instruments to monitor the incoming beam and a 7-element solid state silicon drift detector to measure the fluorescence photons. Data was recorded with SPEC, pre-processed with Igor Pro (Wavemetrics, Lake Oswego USA) and saved in the hierarchical data format (HDF) version 5. The entire thin section was mapped with a 50×50 μm^2 pixel size and 200 ms integration time per pixel. At selected points, XANES spectra at the Tl-L_{III} edge were acquired in step-scan mode. A full XANES scan required 5 minutes (12,558–12,967 eV, 226 points, 5 eV steps in the pre-edge region, 0.6 eV steps around the edge and 2 eV steps after the edge, 1 second integration time per point). Three scans were performed at each position. A pellet of grey Se(0) was recorded between the second and third ionization chamber during all measurements to check the monochromator stability. The photon flux density on the sample was calculated to be between 0.4 and 1×10^8 photons/μm^2/sec (proportional to the decaying electron beam current in the storage ring, which is refilled every 12 hours).

2.4. Synchrotron measurements at the I18 beamline at Diamond

A subarea of 3×3 mm^2 on the thin section was analyzed at beamline I18 of the Diamond Light Source (Didcot, UK) (Mosselmans et al., 2009). This undulator beamline is equipped with a fixed-exit double crystal Si 111 monochromator for energy selection, calibrated in the same way as at SUL-X. Slits combined with Kirpatrick-Baez mirrors were used to focus the X-ray beam to a 5×5 μm^2 spot size on the sample. The section on the Si wafer was glued onto a sapphire disc, inserted into an Oxford Instruments liquid helium cryostat, and cooled down to 10 K for analysis. Data was collected in fluores-

Please cite this article in press as: Marafatto F. F., et al. Thallium sorption by soil manganese oxides: Insights from synchrotron X-ray micro-analyses on a naturally thallium-rich soil. *Geochim. Cosmochim. Acta* (2021), https://doi.org/10.1016/j.gca.2021.03.011

cence mode using a Repic Mic-R20 micro ion chamber to monitor the incoming beam and two 4-element Vortex Si drift detectors (SDD) and XSPRESS-3 acquisition electronics to acquire the fluorescence spectra. Data was processed using the Generic Data Acquisition (GDA) user interface, developed at the Diamond Light Source, and saved into nexus (nxs) hdf5 datasets. Two-dimensional X-ray fluorescence maps were collected on selected areas with a dwell time per pixel of 10 ms at several energies across the Tl-L_{III} edge (12,625, 12,630, 12,658, 12,671, 12,677, 12,686, 12,726, 12,755 eV) that covered diagnostic features in the normalized XANES spectra of key endmember species (Tl(III) on δ-MnO_2 and Tl(I) associated with illite). Ga_2O_3 filters (6 absorption lengths) were placed before the two fluorescence detectors to suppress the fluorescence signal from As. An additional XRF map without Ga_2O_3 filter was collected at an incident photon energy of 15 keV to obtain element distribution data devoid of the filter effect and complementary data on Tl distribution using the Tl K_β fluorescence line. The fluorescence data was saved as full XRF spectra and as multichannel analyzer (MCA) counts for all elements of interest (defined in GDA as the integrated counts over a range of detector channels). On one sample area during a previous beamtime, the chemical mapping was replicated 5 times to evaluate for potential beam induced speciation changes.

2.5. XANES reference spectra for data interpretation

For the analysis of the point XANES spectra collected at the SUL-X beamline at room temperature, the following six reference spectra recorded at room temperature were used: (i) Tl_2O_3 (avicennite) (Voegelin et al. (2015)), (ii) Tl (III) sorbed onto δ-MnO_2 (Na-δ-MnO_2 with 0.21 Tl/Mn; Wick et al. (2019)), (iii) Tl(I) sorbed onto triclinic birnessite (0.15 Tl/Mn; Wick et al. (2019)), (iv) Tl(I)-substituted jarosite (Dutrizac et al. (2005)).

For the analysis of the chemical image stacks recorded at the I18 beamline at a temperature of 10 K, a set of five reference spectra recorded at 20 K at the SAMBA beamline (French National Synchrotron Soleil; Gif-sur-Yvette; France) was used: (i) Tl_2O_3 (avicennite), (ii) Tl(III) sorbed onto δ-MnO_2 (spectrum of sample Na-δ-MnO_2 with 0.015 Tl/Mn; published in Wick et al. (2019)), (iii) Tl(I) sorbed onto triclinic birnessite (sample with 0.016 Tl/Mn from Wick et al. (2019)), (iv) Tl(I)-substituted jarosite (sample from Dutrizac et al. (2005); kindly provided by Susanne Beauchemin), (v) Tl(I) adsorbed at the frayed edges of illite (illite with Tl loading of 3′800 mg/kg Tl(I) from Wick et al. (2018)).

All spectra were aligned to each other based on spectra of Tl_2O_3 or grey Se(0) (Se K-edge) recorded together with the reference spectra, and are plotted together for visual comparison in Fig. S3 of the supporting information.

2.6. Data processing

2.6.1. Point XANES spectra at SUL-X

Point XANES spectra collected at the SUL-X beamline were background subtracted in Athena (Ravel and Newville, 2005) in the same way as the reference spectra (edge energy $E_0 = 12{,}666$ eV; pre-edge background range from 36 to 26 eV before the edge, post-edge normalization range from 15 to 89 eV above the edge, using a linear function to fit the pre-edge range and a cubic function to fit the post-edge range). The point XANES spectra were then corrected for energy shift and evaluated by linear combination fitting (LCF) using Athena, limiting the number of spectra in the fits to 2 and using the combinatorics tool to select the best 2-component fit.

Estimates for the concentrations of Tl, Mn and arsenic (As) on the points of interest (POI) analyzed by XANES were extracted from the raw data files with a custom script, taking advantage of the fact that the raw counts over the energy windows of the Mn Kα, As Kα and Tl Lα fluorescence lines were recorded in the scan files. For Tl, the pre-edge and post-edge counts were averaged in the energy ranges 12,558–12,612 eV (pre-edge) and 12,780–12,800 eV (post-edge) and the net counts were obtained by subtracting the pre-edge from the post-edge signal. For Mn and As, the respective raw counts were averaged over scan energies from 12,780 to 12,800 eV (consistent with the Tl post-edge signal). Because no reference materials were measured for calibration, raw Tl/Mn count ratios were derived from the averaged counts. For selected POI, these count ratios were compared with molar ratios obtained for the same points on a laboratory μ-XRF instrument based on a built-in fundamental parameter algorithm. By linear regression over 7 POI, a scaling factor (0.13) was derived to transform Tl/Mn count ratios into molar ratios (Table S1).

2.6.2. XRF maps

The XRF maps recorded at 15 keV at SUL-X and I18 were analyzed with PyMCA (Solé et al., 2007) to extract deconvoluted peak intensities for selected elements from the full XRF spectra. The redox speciation data was obtained through custom scripts written in Python, version 3.6 (Van Rossum and Drake Jr, 1995). A detailed description of these scripts is provided in the SI (section 2). Briefly, chemical maps were extracted from the hdf5 datasets, aligned based on the As MCA map with an image translation cross-correlation algorithm to the lowest energy map to account for energy-dependent beam drift, and smoothed with a 3×3 pixel moving average (visually deemed as a good compromise between feature identification and noise reduction, see Fig. S4). Pixels where the raw Tl counts above the edge were less than 3 times the Tl counts below the edge were masked and excluded from further analysis.

The Tl MCA counts in the XRF maps used for chemical imaging were first background-corrected by subtracting the counts recorded at the lowest (pre-edge) incident X-ray energy from all maps collected at higher energies. Subsequently, the Tl MCA counts were normalized by dividing the background-corrected counts by the difference between the counts recorded at the highest and the lowest incident X-ray energy. The "reduced" reference spectra (the datapoints of the normalized reference spectra at energies at which the chemical maps were recorded) were treated in the same way, so that the value at the lowest and highest energy was equal to 0 and 1, respectively. These reference

Please cite this article in press as: Marafatto F. F., et al. Thallium sorption by soil manganese oxides: Insights from synchrotron X-ray micro-analyses on a naturally thallium-rich soil. *Geochim. Cosmochim. Acta* (2021), https://doi.org/10.1016/j.gca.2021.03.011

spectra were then used to evaluate each pixel in the chemical imaging maps by least squares fitting with 1 or 2 references (one for Tl(III) and one for Tl(I)). An iterative procedure was used to calculate all possible 1- and 2-component fits. The weight of each reference was constrained between 0 and 1. Fit quality was judged based on the net sum of squared residuals (NSSR). The best 2-component fit was preferred over the best 1-component fit if its NSSR was at least 20% lower. An analysis on the uncertainty of the fit results according to Wielinski et al. (2020) indicated that the dominant oxidation state was correctly identified in about 80% of the pixels (see SI). The fractions of Tl(I) and Tl(III) were obtained by normalizing the weights of the Tl(I) and Tl(III) reference of the best fit by the sum of the fitted weights. This analysis resulted in tiff images where the intensity of each pixel represented the fractions of fit-derived Tl(I) or Tl(III), as well as a CSV file where the data for all pixels (Tl, As, Mn counts, normalized Tl(III)% and component chosen for the fit) was reported in tabulated form. Finally, a function in the script allowed to further subdivide the data into rectangular ROIs in order to facilitate the analysis of particular regions (i.e. individual concretions, background).

To increase the reliability of the Tl speciation evaluated by the chemical redox mapping approach, an independent uncertainty analysis was performed on the dataset according to Wielinski et al. (2019). This analysis indicated that 80% of the pixels in the dataset allowed a correct determination of the predominant oxidation state (i.e., the noise in the data was sufficiently low to allow determination of the Tl oxidation state). Details of this procedure are described in the SI and in Fig. S9.

Because no certified reference materials were measured, X-ray attenuation effects could not be corrected on the XRF data. Instead, we applied a scaling factor to the raw Tl counts in order to obtain Tl/Mn count ratios that roughly matched molar Tl/Mn ratios. This scaling factor was derived by comparing the average MCA Tl/Mn counts for selected concretions with semi-quantitative molar Tl/Mn ratios obtained on the laboratory μ-XRF (Table S1). A large standard deviation in the scaling factor is to be expected, because the lower resolution of the laboratory μ-XRF did not allow us to reliably select all areas chosen in the high resolution data. We refer to the corrected Tl counts as "scaled Tl counts". The scaled Tl counts divided by the uncorrected Mn counts provided a rough estimate of the molar Tl/Mn ratio, hereafter referred to as "Tl/Mn ratio".

3. RESULTS

3.1. Bulk soil characterization and laboratory μ-XRF results

The analyzed soil sample had a pH of 6.9, and total contents of 520 mg/kg Tl, 1400 mg/kg Mn, 50,500 mg/kg Fe and 1290 mg/kg As. The pseudo-porewater extract contained 37 μg/L Tl. In terms of total element contents, the sample from 38 cm depth ranged between the samples from 20-40 cm and 60–80 cm depth in the same soil profile that have been described previously (Voegelin et al., 2015). Based on bulk XAS, the sample from 20-40 cm depth (260 mg/kg Tl) was previously found to contain ~93% Tl (I) associated with illite, and ~7% Tl(III). The sample from 60-80 cm depth (1800 mg/kg Tl) was found to contain ~32% Tl(I)-illite together with ~32% Tl(I)-jarosite (i.e., Tl(I) substituting K in jarosite, $KFe_3(OH)_6(SO_4)_2$) and ~36% Tl(III) (probably Tl_2O_3), indicating a higher fraction of secondary Tl-bearing minerals formed by the weathering of the primary mineralization. Based on the Tl content of the bulk sample PI38, its speciation was assumed to be closer to the speciation of the sample from 20-40 cm depth which is dominated by Tl(I)-illite and a minor fraction of Tl(III). By sequential extraction, 7.0% of the total Tl in soil sample PI38 was found to be NH_4-exchangeable and 3.6% to be (reductively) extractable by hydroxylamine at pH 6.1. The molar Tl/Mn ratio in the hydroxylamine extract equaled 0.0065. The analysis of the 1×1 cm^2 thin-section used for the synchrotron measurements by laboratory μ-XRF confirmed the association of elevated Tl contents with Mn concretions, and the semi-quantitative analysis of the cumulative μ-XRF spectrum obtained by integration over the Mn concretions returned a molar Tl/Mn ratio of 0.0066 (SI section 1) in good agreement with the molar Tl/Mn ratio of 0.0065 from the hydroxylamine extract.

3.2. Analysis of 10×10 mm^2 area by μ-XRF and μ-XANES with 60×30 μm^2 resolution

Fig. 1 summarizes the results obtained at the SUL-X beamline for the entire area of the thin section. Fig. 1A and B show the elemental distribution of Mn and Tl. It can be seen that Mn is mostly present in concretions and absent in the background. Variations in the Mn intensity in concretions mostly reflect varying levels of Mn oxide accumulation within the clayey soil matrix. Thallium, on the other hand, is present throughout the clayey soil matrix. Accumulations of Tl can be observed in some regions high in Mn. However, in some locations, high Tl concentrations occur in the absence of Mn, pointing to the presence of Tl-rich species other than Tl associated with Mn oxides. Using a mask to separate pixels associated with Mn concretions from pixels associated with the background soil matrix (without Mn), 9.1% of the total Tl counts were found to be co-localized with soil Mn concretions. If the average count rate in the background soil matrix was subtracted from the counts of each pixel to correct for Tl in clay minerals, the total accumulated counts associated with Mn oxides corresponded to 5.8% the total Tl counts. Qualitatively, this fraction is in a similar range as the 3.6% of the Tl that was extractable with hydroxylamine.

To assess the local speciation of Tl, 40 points of interest (POIs) over the entire thin section were selected for analysis by point XANES spectroscopy (marked in Fig. 1A, B). Comparison of 3 consecutive scans provided no evidence for radiation induced speciation changes on the probed POIs. All XANES spectra were evaluated by LCF using the reference spectra shown in Fig. 1C. The complete LCF results are listed in Table S2, the XANES spectra of selected POIs that cover the observed variation are shown in Fig. 1C, together with the LCF results and spectra.

Please cite this article in press as: Marafatto F. F., et al. Thallium sorption by soil manganese oxides: Insights from synchrotron X-ray micro-analyses on a naturally thallium-rich soil. *Geochim. Cosmochim. Acta* (2021), https://doi.org/10.1016/j.gca.2021.03.011

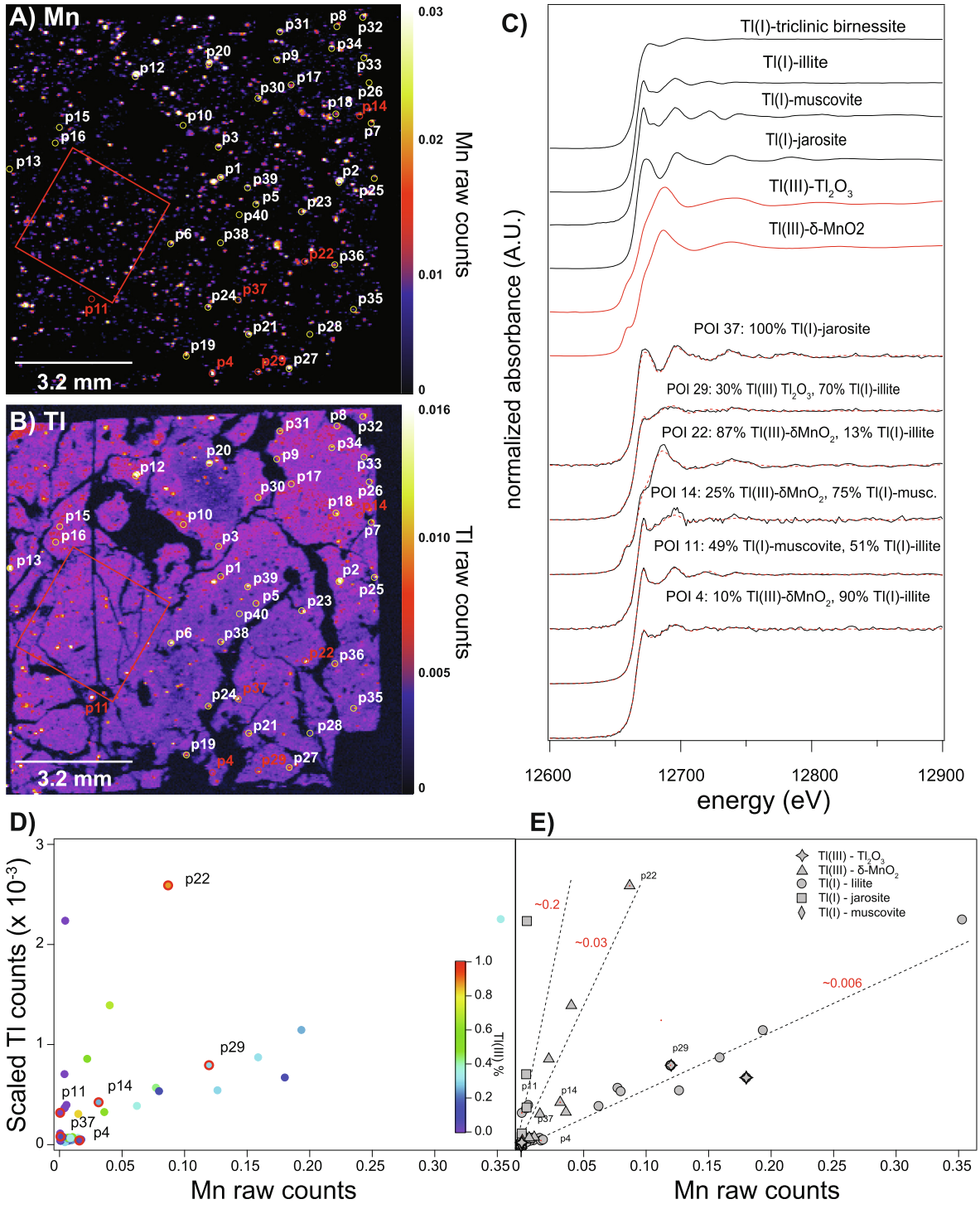

Fig. 1. μ-XRF and μ-XANES data recorded with 60 × 30 μm X-ray beam at room temperature at SUL-X. (A, B) Distribution maps of Mn and Tl obtained by deconvolution of XRF spectra. Points p1 to p39 were analyzed by μ-XANES. Area marked with red square was analyzed by chemical imaging with 5-μm X-ray beam at I18. (C) Reference spectra and selected μ-XANES spectra (black lines) together with LCF spectra (red lines). Scaled Tl counts versus corrected Mn counts for all POI. In (D), color indicates the LCF-derived fraction of Tl(III), in (E), symbol shape indicates the dominant species in the LCF (>50%). (For interpretation of the references to colour in this figure legend, the reader is referred to the web version of this article.)

Of the spectra shown in Fig. 1C, the spectrum of POI 22 was fit with a considerable fraction of Tl(III) on δ-MnO_2. The comparison of the corresponding XANES with the reference spectra of $Tl(III)_2O_3$ and Tl(III) on δ-MnO_2 supported the finding that POI 22 is better described by Tl (III) on δ-MnO_2 than by Tl_2O_3, the former being character-

Please cite this article in press as: Marafatto F. F., et al. Thallium sorption by soil manganese oxides: Insights from synchrotron X-ray micro-analyses on a naturally thallium-rich soil. *Geochim. Cosmochim. Acta* (2021), https://doi.org/10.1016/j.gca.2021.03.011

ized by a smoother absorption edge and pre-edge than Tl_2O_3 (Fig. 1C). For POI 29, the LCF returned 70% Tl(I) and 30% Tl(III), the latter fraction fitted as Tl_2O_3. This species, in contrast to Tl(III) on δ-MnO_2, may be either a residual secondary Tl mineralization associated with Mn that has been observed at depths of 140 cm in this soil profile (Voegelin et al., 2015), or a fitting artifact due to the limited sensitivity of Tl L_{III}-edge XANES to different Tl(III) species in the presence of a major fraction of Tl(I). POI 11 corresponded to a Tl-rich particle low in Mn. Its spectrum could be fit by Tl(I)-illite and Tl(I)-muscovite, suggesting that POI 11 represented an isolated larger micaceous mineral grain enriched in Tl. POI 37 corresponded to Tl(I)-jarosite, a previously identified weathering product of the primary mineralization at the study site (Herrmann et al., 2018; Voegelin et al., 2015). In general, the speciation results derived from point XANES data were in line with previous work on the Erzmatt site, which showed that Tl (I) associated with micaceous clay minerals dominated pedogenic Tl speciation in topsoils, that Tl(III) occurred in Mn concretions, and that Tl(I)-jarosite occurred in some soil horizons as weathering products of a primary Tl-As-Fe-sulfide mineralization (Voegelin et al., 2015).

In Fig. 1D and E, the LCF-derived Tl speciation is shown as a function of the scaled Tl counts plotted against the raw Mn counts of the individual POIs. LCF-derived Tl (III) fractions plotted against total Tl and Mn counts (Fig. 1D) indicated no clear relationship. On the other hand, the majority species plotted against the molar Tl/Mn ratios suggest that Tl(III) fractions tended to be associated with higher Tl/Mn ratios, associated with a shift from Tl(I) predominantly associated with clay minerals to Tl(III) associated with Mn-oxides. At POIs rich in Tl and low in Mn, with Tl/Mn ratios above ~0.2, Tl(I) dominated in the fits and was represented mostly by the Tl(I)-jarosite reference.

These results provide an overview of the soil in terms of elemental distribution and Tl species present, given the high quality of the spectra obtained and the low photon dose, which reduced the risk of irradiation artifacts. Because most concretions are covered by only a limited number of pixels, however, these measurements provide no information on potential variations in Tl loading and redox speciation between and within Mn concretions. A sub-area was therefore selected (marked in Fig. 1A, B) to perform additional measurements at higher resolution with a 5×5 μm^2 X-ray beam.

3.3. Analysis of 3×3 mm^2 area by chemical imaging with 5×5 μm^2 resolution

The higher resolution measurements at beamline I18 at Diamond were carried out with a 2–3 orders of magnitude higher photon flux density on the sample. Despite sample cooling to 10 K, this higher photon flux density enhanced X-ray induced speciation changes, namely the reduction of Tl(III) to Tl(I) when collecting XANES spectra with dwell times of several tens of seconds on one spot. In line with this observation in a natural sample, a test with Tl_2O_3 embedded in cellulose pellets that were analyzed at 100 K showed that the rate of beam-induced Tl(III) reduction substantially increased when the X-ray beam was focused to smaller sizes and the X-ray photon flux density increased (Fig. S11).

To gain spatially-resolved information on Tl redox speciation over an entire sample area and individual concretions, an alternative approach using chemical imaging was therefore adopted which also considerably reduced sample exposure time. Tests in which the chemical imaging on a given sample area (on another thin section) was repeated 5 times, corresponding to ~5 s total exposure time (slightly higher because of partial beam overlap in adjacent pixels), revealed no evidence for beam-induced Tl(III) reduction (Fig. S12), suggesting that the chemical imaging data was not affected by beam damage.

The results from element distribution mapping and chemical imaging of a subarea of the thin section are shown in Fig. 2, with additional elements shown in Fig. S2. As seen in the data collected at SUL-X, Mn levels in the soil matrix are very low, and Mn mainly occurs in concretions that vary in size and extent of Mn accumulation. High levels of Tl are in most instances associated with Mn concretions, although there are also some points with high Tl but low Mn. In contrast to Mn, a constant background of Tl was also observed throughout the soil matrix (Fig. 2A, B). The distribution map for Tl(III) clearly shows that Tl in the soil matrix is dominantly Tl(I), with 94% of the Tl(I) pixels fit by the Tl(I)-illite reference and 6% fit by Tl(I)-jarosite, whereas Tl(III) is mainly found in association with Mn concretions (Fig. 2D). The fraction of Tl(III) in the entire sampled area was calculated to be 8% (sum of Tl counts from Tl(III) / sum of Tl counts in all pixels), with 86% of this area fitted by Tl(III) in δ-MnO_2 and the remaining 14% as Tl(III) in Tl_2O_3.

The plot of Tl versus Mn counts with color-coded symbols based on Tl redox speciation (Fig. 2C) shows that the data can be divided into several domains: (i) Pixels with high Tl and low Mn counts, mostly corresponding to small Tl(I)-jarosite grains (Fig. S5) as also observed in the data from SUL-X (Fig. 1E); (ii) Pixels with high Mn and low Tl counts, mostly corresponding to Tl(I)-illite/muscovite (Fig. S5); (iii) Intermediate region where the Tl(III) fraction increases with increasing Tl concentration and increasing Tl/Mn ratios. To further characterize these domains, selected ROIs were examined in greater detail. The results for three ROIs (2, 3, 4) featuring Mn concretions with different average Tl/Mn ratios (marked in green in Fig. 2A, B, D) are shown in Figs. 3, 4 and 5. The respective data for ROI 1 (soil matrix with Tl(I) associated with clay minerals) and ROI 5 (jarosite grain) are shown in the supporting information (Fig. S5). Average spectra for ROIs 2, 3 and 4 are also shown compared with the spectra of the main phases fitted in Fig. S6.

A Mn concretion with intermediate Tl/Mn ratio (ROI 2) is shown in Fig. 3. The close correlation between Tl and Mn counts suggested that the accumulation of Tl was indeed due to Tl sorption onto Mn oxides, and that the Tl loading of the Mn oxide(s) was fairly homogeneous throughout the concretion. Data shown in Fig. 3C, D indicated a substantial accumulation of Tl(III) in this concretion, but because the accumulated Tl did not vastly exceed background Tl

Please cite this article in press as: Marafatto F. F., et al. Thallium sorption by soil manganese oxides: Insights from synchrotron X-ray micro-analyses on a naturally thallium-rich soil. *Geochim. Cosmochim. Acta* (2021), https://doi.org/10.1016/j.gca.2021.03.011

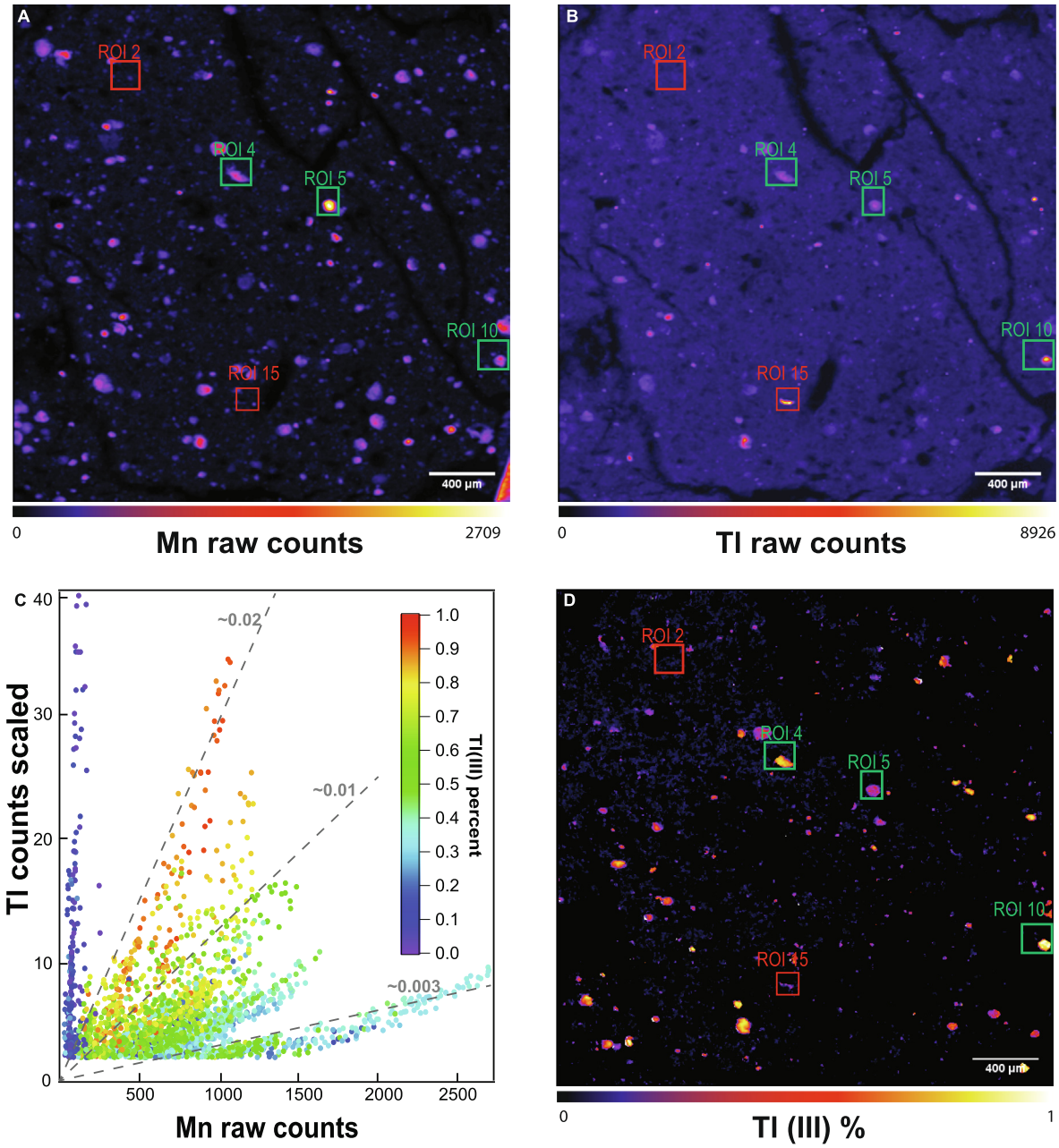

Fig. 2. µ-XRF and chemical imaging data recorded with 5-µm X-ray beam at 10 K at I18. (A, B) Mn and Tl XRF maps collected at 15 keV (deconvoluted peak intensities) over sub-area marked in red in Fig. 1. In both maps, contrast adjusted to 80% of the maximum intensity. (C) Tl scaled counts (according to Table S2) versus Mn raw counts, color-coded according to LCF-derived Tl(III) fraction. Lines depicting various molar Tl/Mn ratios are shown to guide the eye. (D) LCF-derived fraction of Tl(III) over mapped area, where black pixels indicate those masked out by the edge-step filter described in the text. All maps were obtained by smoothing the data with a 3 × 3 moving average. In panels A, B D, the green squares depict ROIs 2, 3 and 4 that are shown in detail in Figs. 3, 4 and 5, respectively, and the red squares the ROIs shown in Fig. S5. (For interpretation of the references to colour in this figure legend, the reader is referred to the web version of this article.)

levels, the Tl redox speciation also included the signal from Tl(I) in soil clay minerals. In Fig. 6 (panel A), we therefore plotted the LCF-derived fraction of Tl(III) in each pixel of ROI 2 as a function of the Tl counts, and in comparison to the fraction of Tl counts in each pixel above the background counts (minimum pixel count in masked out area). Assuming that the background counts account for Tl(I) in soil clay minerals, the close match of the Tl(III) fractions and the accumulated Tl count fractions clearly indicated that Tl accumulated in the Mn concretion in ROI 2 was nearly exclusively Tl(III) (Fig. 6A). Similar results as for the ROI 2 were obtained for a concretion on another section that was analyzed by chemical imaging in an earlier beamtime at the same beamline (Fig. S7).

Fig. 4 shows another Mn concretion (ROI 3) with a similarly close correlation between Tl and Mn counts as in the

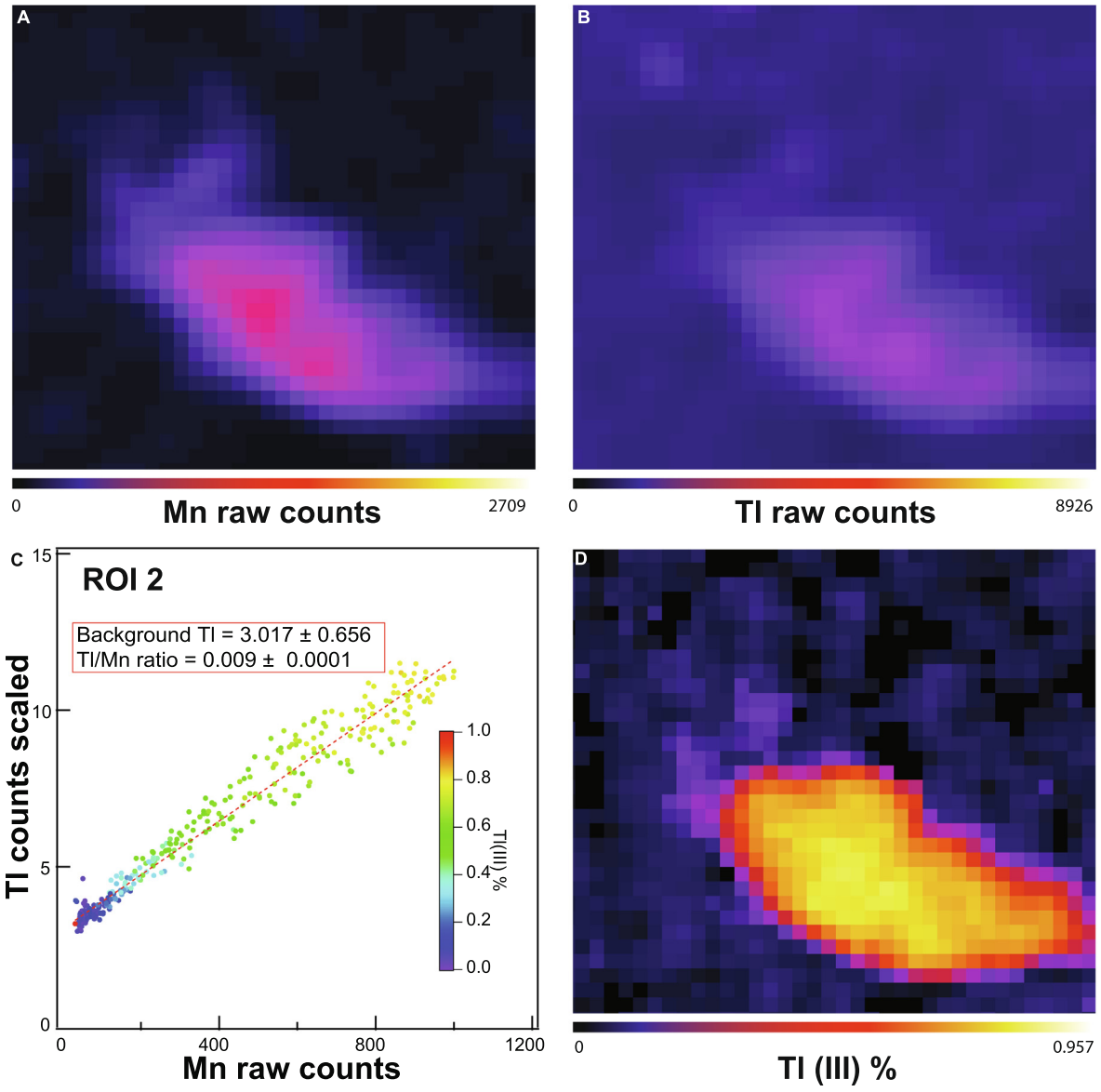

Fig. 3. μ-XRF and chemical imaging data for ROI 2. (A, B) Mn and Tl XRF maps. (C) Tl versus Mn counts, color coded based on LCF-derived Tl(III) fractions. (D) Map of LCF-derived Tl(III) fractions. Black pixels in (D) indicate areas excluded by the Tl "edge step" mask. (For interpretation of the references to colour in this figure legend, the reader is referred to the web version of this article.)

concretion shown in Fig. 3, but with a lower Tl/Mn ratio (similar Tl counts but higher Mn counts than in ROI 2). In this concretion, the highest LCF-derived Tl(III) fractions reached only about 30% (Fig. 4C), and the comparison of Tl(III) fractions with accumulated Tl fractions suggested that only about half of the accumulated Tl was Tl(III), the other half Tl(I) (Fig. 6B).

The Mn concretion with the highest Tl/Mn ratio and the highest Tl counts in the mapped area (ROI 4) is shown in Fig. 5. In this concretion, the highest Tl loadings exceeded background Tl levels tenfold, rendering the contribution of background Tl(I) in clay minerals negligible. At these elevated Tl loadings, Tl was identified as nearly 100% Tl (III). At intermediate Tl levels, the LCF-derived Tl(III) fraction exceeded the fraction of Tl counts above background (Fig. 6C), which could indicate that the background signal from Tl(I)-bearing clay minerals within this concretion was lower than in the surrounding soil matrix.

4. DISCUSSION

4.1. Extent of Tl association with Mn oxides in Erzmatt soils

The chemical imaging performed in this work showed that clay-associated Tl(I) occurs finely dispersed in the soil matrix (Fig. 2D). This observation is in line with a recent study on the sorption and speciation of Tl in Erzmatt soils, which concluded that most of the Tl was firmly bound in the interlayers of micaceous clay minerals (Wick et al., 2020). Regarding the association of Tl with soil Mn oxides,

Please cite this article in press as: Marafatto F. F., et al. Thallium sorption by soil manganese oxides: Insights from synchrotron X-ray micro-analyses on a naturally thallium-rich soil. *Geochim. Cosmochim. Acta* (2021), https://doi.org/10.1016/j.gca.2021.03.011

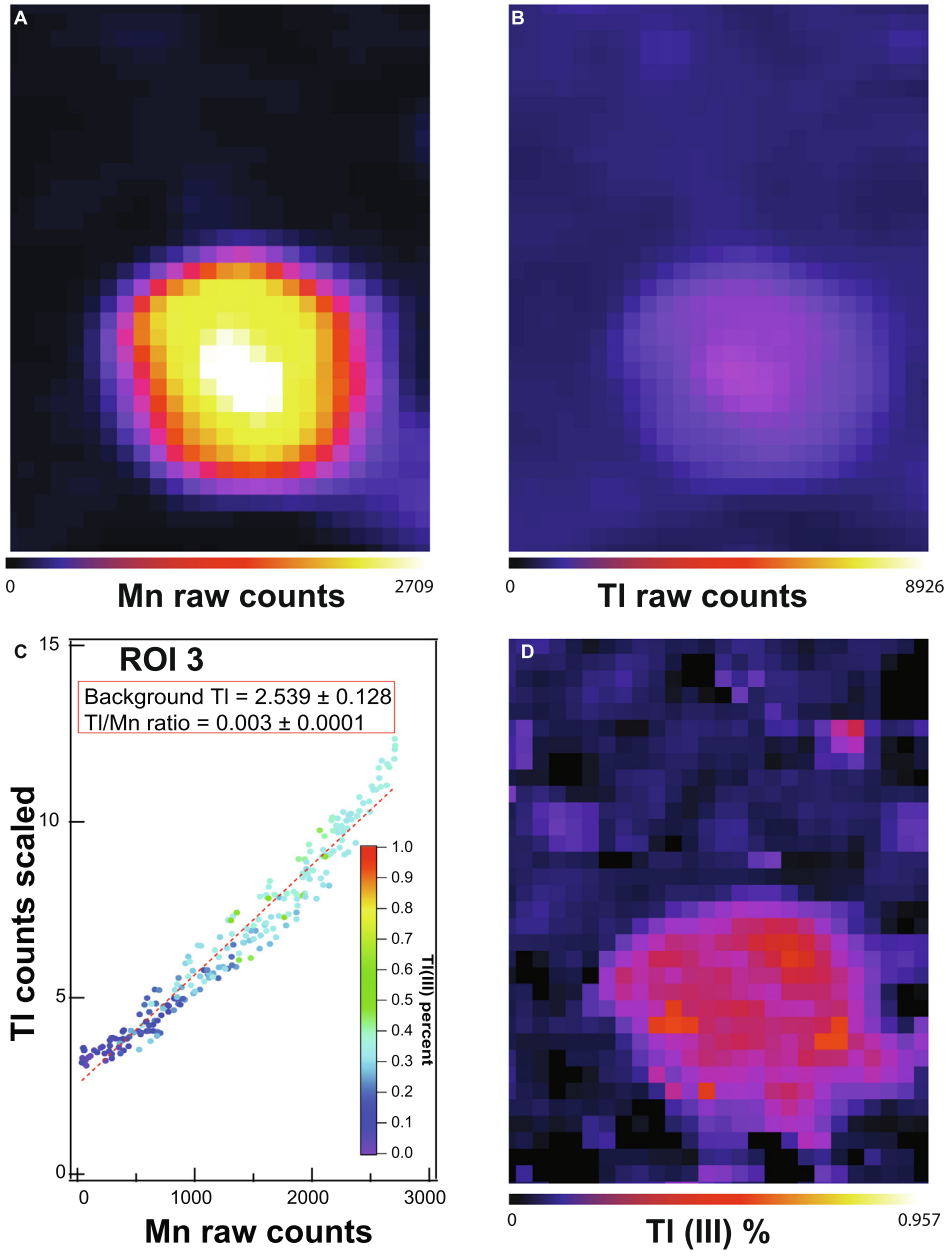

Fig. 4. μ-XRF and chemical imaging data for ROI 3. (A, B) Mn and Tl XRF maps. (C) Tl versus Mn counts, color coded based on LCF-derived Tl(III) fractions. (D) Map of LCF-derived Tl(III) fractions. Black pixels in (D) indicate areas excluded by the Tl "edge step" mask. (For interpretation of the references to colour in this figure legend, the reader is referred to the web version of this article.)

the micro-XRF analyses clearly revealed the close spatial association of elevated Tl levels with high Mn contents in soil Mn concretions, which points to the preferential uptake of Tl by Mn oxides (Figs. 1-5). From the synchrotron data collected at SUL-X, it was estimated that 5.8% of the total Tl in the probed thin section was associated with Mn oxides in concretions, in fair agreement with the 3.6% of the total Tl that were reductively extractable with hydroxylamine from the corresponding bulk soil sample. This percentage in turn fell into the range of 0.4% to 6.2% hydroxylamine-extractable Tl recently reported for 18 topsoil materials from Erzmatt (average: 2.0%±1.3%) (Wick et al., 2020). As discussed in this recent study, the fractions of Tl associated with soil Mn oxides in Erzmatt topsoil samples are nearly as high as the fractions of readily exchangeable soil Tl(I), which is mostly associated with soil clay minerals. In Erzmatt, the high fractions of Tl fixed in clay minerals may be attributed to the geogenic origin of Tl and its incorporation into clay minerals over the course of soil formation. We therefore postulate that in freshly (anthropogenically) contaminated soils, larger fractions of the Tl released from primary Tl-bearing contaminant phases may still be retained in readily exchangeable form or by sorption onto Mn oxides.

Please cite this article in press as: Marafatto F. F., et al. Thallium sorption by soil manganese oxides: Insights from synchrotron X-ray micro-analyses on a naturally thallium-rich soil. *Geochim. Cosmochim. Acta* (2021), https://doi.org/10.1016/j.gca.2021.03.011

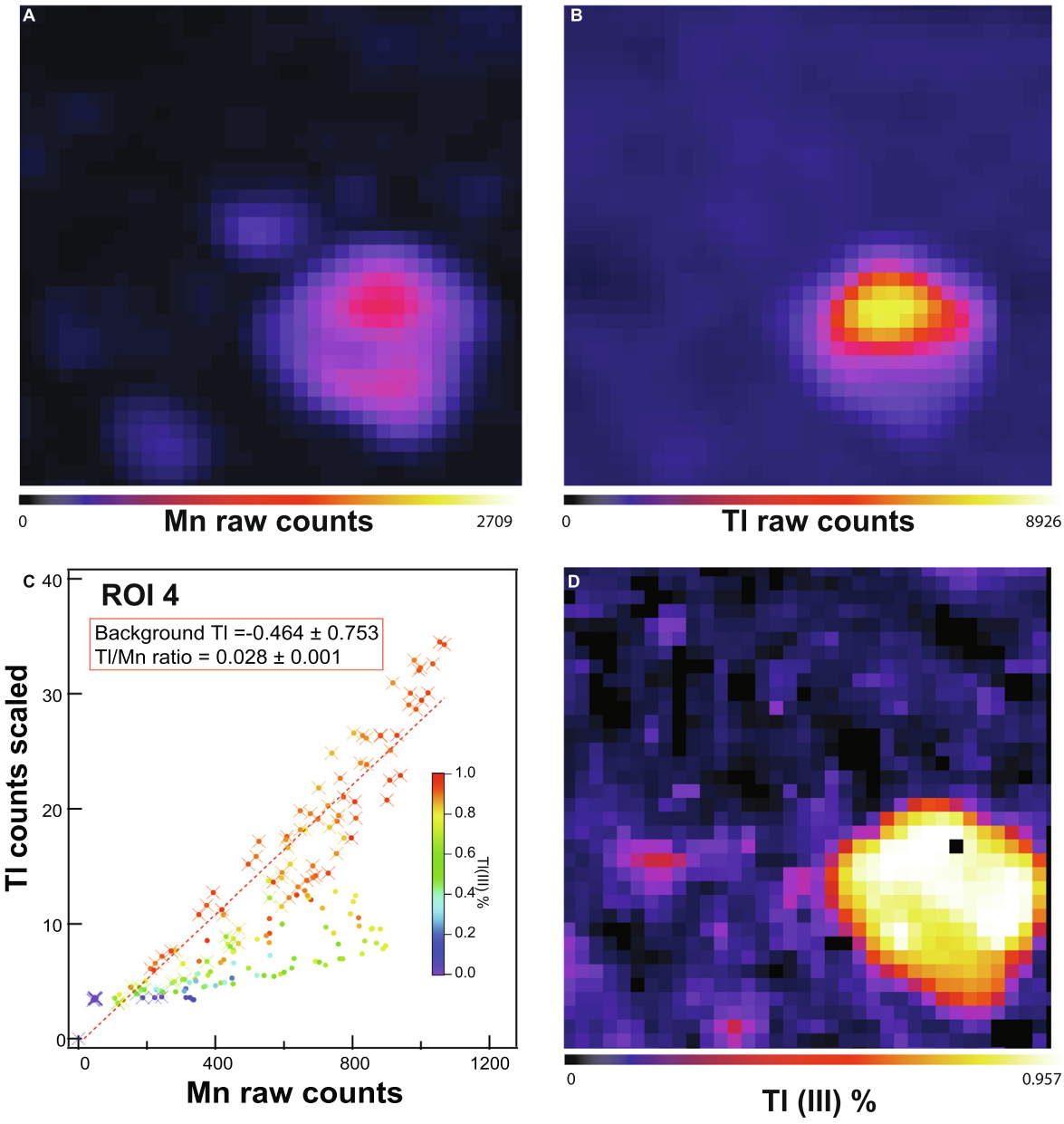

Fig. 5. μ-XRF and chemical imaging data for ROI 10. (A, B) Mn and Tl XRF maps. (C) Tl versus Mn counts, color coded based on LCF-derived Tl(III) fractions. The crosses indicate the datapoints included for the linear regression. (D) Map of LCF-derived Tl(III) fractions. Black pixels in (D) indicate areas excluded by the Tl "edge step" mask. (For interpretation of the references to colour in this figure legend, the reader is referred to the web version of this article.)

4.2. Mode of Tl uptake by Mn oxides in Erzmatt soils

Soil Mn concretions in the Erzmatt soils in general are closely associated with the clayey soil matrix. Therefore, spectral contributions from clay-associated Tl(I) complicated the assessment of the redox speciation of Tl accumulated in Mn oxides. Nevertheless, the analysis of the Tl redox speciation in individual Mn concretions with very high Tl levels (dominated by Mn oxide sorbed Tl) by Tl L_{III}-edge XANES spectroscopy confirmed that Tl was mainly Tl(III). The chemical imaging of an entire area as well as a sub-area on a second, separate thin section (Fig. S7) further supported the conclusion that accumulated Tl in soil Mn concretions was primarily Tl(III), although some concretions also accumulated Tl(I) (Figs. 4 and S7). Laboratory studies on the sorption of Tl by synthetic Mn oxides show that highly selective oxidative Tl uptake is restricted to hexagonal birnessite, a phyllomanganate, with uncapped vacancy sites in its octahedral sheets (Peacock and Moon, 2012; Wick et al., 2019). In contrast, hexagonal birnessite with Mn(III)-capped vacancies, triclinic birnessite with vacancy-free Mn(III)-containing octa-

Please cite this article in press as: Marafatto F. F., et al. Thallium sorption by soil manganese oxides: Insights from synchrotron X-ray micro-analyses on a naturally thallium-rich soil. *Geochim. Cosmochim. Acta* (2021), https://doi.org/10.1016/j.gca.2021.03.011

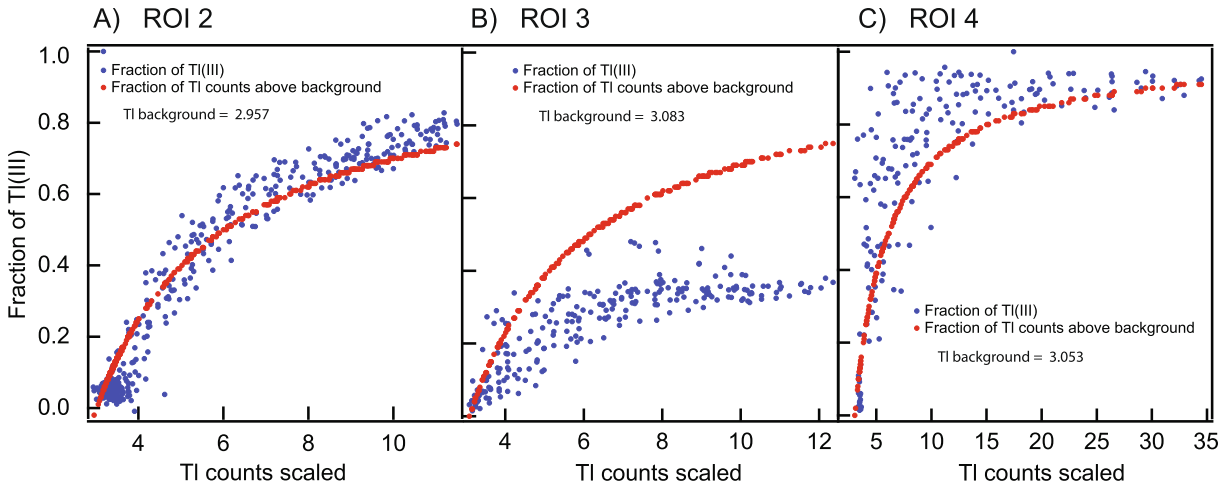

Fig. 6. LCF-derived fraction of Tl(III) plotted vs the Tl counts, scaled by the scaling factor described in the text for ROIs 2 (A), 3 (B) and 4 (C). In blue are the datapoints of the pixels within a ROI, in red are the calculated datapoints if the pixels related to the background (calculated based on the lowest Tl count within the selected area, which included also some background pixels, which were 2.957, 3.083 and 3.053 for A, B, C respectively) were subtracted to the data. (For interpretation of the references to colour in this figure legend, the reader is referred to the web version of this article.)

hedral sheets, or tectomanganates like todorokite or cryptomelane lack the capacity to oxidize Tl and sorb Tl(I) as Tl(I) with a lower sorption affinity (Wick et al., 2019). The accumulation of Tl(III) in soil Mn concretions in Erzmatt topsoil samples is therefore primarily attributed to the oxidative scavenging of Tl by vacancy-containing hexagonal birnessite. This conclusion is supported by the first microspectroscopic study on Erzmatt soils by Voegelin et al. (2015), in which the Tl in one soil Mn concretion was unequivocally identified as Tl(III) sorbed onto hexagonal birnessite using extended X-ray absorption fine structure (EXAFS) spectroscopy. Oxidative uptake of Tl by hexagonal birnessite is also expected to cause an enrichment of heavier ^{205}Tl relative to ^{203}Tl (Nielsen et al., 2013; Peacock and Moon, 2012). Therefore, the finding that Mn oxides in Erzmatt soils bind Tl mainly as Tl(III) supports the conclusion of a recent stable Tl isotopes study on two soil profiles on the Erzmatt in which the enrichment of ^{205}Tl in the uppermost B-horizons relative to the unweathered subsoil horizons was attributed to periodic oxidative Tl scavenging by soil Mn oxides (Vaněk et al., 2019).

4.3. Solubility of Tl associated with soil Mn oxides in Erzmatt soils

Based on the Tl/Mn molar ratio of 0.0065 derived from the hydroxylamine extraction targeting Mn oxides and associated Tl (in line with the average Tl/Mn molar ratio in soil Mn concretions derived from laboratory μ-XRF), an average Tl content in soil Mn oxides of ~11,800 mg/kg can be derived. In relation to a dissolved Tl concentration of 37 μg/L (1.8×10^{-7} M) in the pseudo-porewater $CaCl_2$ extract, this loading corresponds to a log-scale distribution coefficient for Tl sorbed onto soil Mn oxides (log (K_d/(L/kg)) of 5.5, close to the average log K_d value of 5.2 (±0.3) determined for 18 topsoil samples from the Erzmatt using the same protocol (Wick et al., 2020). For the same dissolved Tl concentration of 37 μg/L, a log K_d value of 6.4 can be estimated for Tl sorption onto δ-MnO_2 from sorption isotherm parameters reported for Tl sorption onto δ-MnO_2 (in Na, K or Ca electrolyte) (Wick et al., 2019; Table 2). Both the soil-derived and the isotherm-derived log K_d values apply to conditions where Tl sorption is dominated by oxidative Tl uptake onto birnessite. The roughly one unit lower soil-derived log K_d value probably reflects that sorption competition with other major and trace metal cations on vacancy sites limits oxidative Tl scavenging in soils. Considering that soil Mn concretions may also contain less reactive Mn oxides (and Fe oxides) that sorb Tl(I) without oxidation, the dominance of Tl(III) in soil Mn concretions may also reflect that competing cations effectively inhibit non-oxidative sorption of Tl(I). In any case, the comparison indicates that sorption data obtained on synthetic δ-MnO_2 cannot be directly used to estimate the extent of Tl uptake by soil Mn oxides, and that both the formation and mineralogy of Mn oxides in soil Mn concretions and the competition of major and trace element cations for highly reactive sorption sites on hexagonal birnessite under environmentally relevant conditions warrant further study.

The conditional soil-derived log K_d value of 5.2 for oxidative Tl uptake by soil Mn oxides is about 2 log units higher than the log K_d of ~3.3 for Tl sorption onto illite in competition with major cations in soil porewater that has been calculated from laboratory sorption experiments (Wick et al., 2018; Fig. 2F). This difference reflects an about 2 orders of magnitude higher sorption affinity for oxidative Tl uptake by Mn oxides in Erzmatt soils than for cation exchange of Tl(I) on micaceous clay minerals. Thus, in a soil with ~0.1% (w/w) Mn oxides and ~10% micaceous clay minerals, about similar amounts of Tl would be retained via the two sorption mechanisms, as has been observed for a larger set of topsoil samples from the Erzmatt (Wick et al., 2020).

Please cite this article in press as: Marafatto F. F., et al. Thallium sorption by soil manganese oxides: Insights from synchrotron X-ray micro-analyses on a naturally thallium-rich soil. *Geochim. Cosmochim. Acta* (2021), https://doi.org/10.1016/j.gca.2021.03.011

4.4. Formation of Tl-enriched soil Mn concretions in Erzmatt soils

Soil Mn concretions typically form by microbially catalyzed or autocatalytic oxidation of Mn(II) to insoluble Mn(IV) (Sposito, 2008; Tebo et al., 2004). Freshly formed Mn oxides in aquatic and terrestrial systems have been characterized as vacancy-containing hexagonal birnessites with a minor fraction of Mn(III), partly in their octahedral sheets, partly in the interlayers capping vacancy sites (Tebo et al., 2004; Villalobos et al., 2005; Webb et al., 2005). They are highly reactive and can effectively sequester trace elements via non-oxidative (Pena et al., 2015; Toner et al., 2006) and oxidative sorption mechanisms (Kim et al., 2002; Simanova and Pena, 2015), including Tl (Peacock and Moon, 2012, Wick et al., 2019). Over time, fresh hexagonal birnessite can transform into less reactive Mn oxides such as triclinic birnessite or tectomanganates, depending on the presence of sorbed cations (Bodei et al., 2007; Grangeon et al., 2014) and soil organic matter (Remucal and Ginder-Vogel, 2014) that may inhibit or direct these transformations. Regarding the predominant oxidative uptake of Tl(III) by soil Mn oxides in the Erzmatt soils, it is probable that this process mainly occurs when dissolved Tl(I) in soil pore water reacts with freshly formed hexagonal birnessite. Variations in the Tl/Mn ratios of soil Mn concretions that contain mainly Tl(III) (e.g., ROI 2 and 4) and the identification of concretions that also accumulate Tl(I) (ROI 3) may reflect differences in the soil chemical conditions during birnessite precipitation, for example in the concentration of dissolved Tl(I) or the concentrations of other competing cations. In a study on the uptake of Tl by soil ferromanganese nodules, only about half of the sorbed Tl was Tl(III), and this observation was attributed to competitive sorption of metal cations on vacancy sites (Peacock and Moon, 2012). Soil Mn concretions in Erzmatt soils may also have formed over different periods of time (and soil reduction/oxidation cycles) and may therefore contain variable proportions of fresh hexagonal birnessite, less reactive Mn oxide transformation products, as well as Fe oxides, which may affect both the Tl/Mn ratios as well as the fractions of accumulated Tl(III) and Tl(I).

In earlier studies on Erzmatt soil, Tl_2O_3 (avicennite) was identified as a weathering product of the primary metal sulfide mineralization (Herrmann et al., 2018; Voegelin et al., 2015). Individual Tl_2O_3 particles were observed to feature coatings of Mn, presumably Mn oxides. These coatings could form by a redox reaction of dissolved Mn^{2+} with Tl_2O_3 minerals grains (Voegelin et al., 2015) (according to the overall reaction $2Mn^{2+} + Tl_2O_3 + H_2O = 2MnO_2 + 2Tl^+ + 2H^+$), a process that could ultimately lead to the complete replacement of entire Tl_2O_3 grains by Mn oxides enriched in Tl. For several reasons, however, we believe that this process is negligible in the studied soil sample: (i) The sample was not from the most heavily mineralized soil horizons where Tl_2O_3 has previously been identified; (ii) An anti-correlation between Tl and Mn rather than a correlation would be expected for Mn oxide-coated Tl_2O_3 grains; (iii) MnO_2 formed by a redox reaction of Mn^{2+} with Tl_2O_3 would be expected to be highly loaded with Tl(I). However, further work is required to assess the potential importance of this process in mineralized soil horizons at the Erzmatt site.

4.5. Environmental implications

The microspectroscopic results obtained on a naturally Tl-rich soil sample from the Erzmatt site suggest that the high levels of Tl in soil Mn concretions are primarily due to the oxidative uptake of Tl by vacancy-containing hexagonal birnessite. Similarly, an earlier spectroscopic study indicated that the enrichment of Tl in marine ferromanganese crusts was controlled by the oxidative Tl scavenging by hexagonal birnessite (Peacock and Moon, 2012). In line with these observations on natural samples, laboratory sorption data showed that oxidative Tl uptake by vacancy-containing hexagonal birnessite is much more selective than non-oxidative Tl binding by other Mn oxides (Wick et al., 2019).

In general, the importance of Mn oxides for Tl sorption in soils and sediments critically depends on their mineralogy and their abundance in relation to other sorbents, especially micaceous clay minerals, as well as on the competitive sorption of other major and trace metal cations. In soils, oxidative uptake of Tl by Mn oxides is expected to be most relevant under conditions where reactive vacancy-containing birnessite is freshly formed in the presence of dissolved Tl, for example as a consequence of periodic waterlogging and related soil reduction / re-oxidation events. The periodic reductive dissolution of Mn oxides or the transformation of reactive into less reactive Mn oxides may induce changes in the solubility of Tl over soil reduction-oxidation cycles, but may also limit the ability of Mn oxides to act as long-term sorbents for a large fraction of Tl in soils. Whereas the incorporation of Tl into micaceous clay minerals may dominate Tl sequestration in soils in the long term, as observed in the naturally Tl-rich soils on the Erzmatt, oxidative Tl uptake may be especially relevant in anthropogenically contaminated soils that experienced relatively recent inputs of Tl.

This study documents the importance of highly selective oxidative Tl uptake by vacancy-containing birnessite in soil Mn concretions. Nevertheless it should be noted that non-oxidative Tl uptake by other Mn oxides exhibits a rather high selectivity as well when compared to Tl uptake by other sorbent phases. Therefore, under conditions where massive Mn oxide accumulations form, for example in the oxidation zones of mineral deposits, also non-oxidative Tl uptake by Mn oxides can be an important Tl sequestration mechanism.

To advance the mechanistic and quantitative understanding of how different Mn oxides affect Tl sorption, solubility and dynamics in soils and sediments under varying biogeochemical conditions, further studies on the extent and mode of Tl association with natural Mn oxides in different types of environments, on the effect of Mn oxides on Tl speciation and solubility in (redox-)dynamic environmental systems, as well as on the adsorption of Tl onto pure (synthetic) Mn oxides in the presence of competing cations under well-constrained laboratory conditions are needed.

Please cite this article in press as: Marafatto F. F., et al. Thallium sorption by soil manganese oxides: Insights from synchrotron X-ray micro-analyses on a naturally thallium-rich soil. *Geochim. Cosmochim. Acta* (2021), https://doi.org/10.1016/j.gca.2021.03.011

4.6. Classical μ-XRF / XAS versus chemical imaging analysis

As synchrotron upgrades (i.e. diffraction-limited storage rings) result in considerable increases in spatial resolution and photon flux density at microfocused beamlines, the traditional approach of spatially-resolved speciation studies that combines XRF mapping with subsequent point XAS measurements at selected locations may become inadequate to investigate radiation sensitive environmental samples (i.e. Fig. S11) (Lombi and Susini, 2009). Although the spatial resolution of microanalytical XRF/XAS studies at second generation synchrotron lightsources may be limited, the reduced photon flux may allow the collection of full XANES or even EXAFS spectra with data acquisition speeds that are within the limits of beam damage, and thereby to identify and characterize unknown element species in complex samples (Kretzschmar et al., 2012; Manceau et al., 2007; Peacock and Moon, 2012). On the other hand, many environmental processes occur on the micrometer scale (Parise and Brown, 2006), which may be missed and lead to errors in interpretation when using a larger beam. Additionally, the user-defined selection of points of interest with the traditional approach may miss important features that cannot be investigated in the dataset once the beamtime is over. With the chemical redox mapping approach, the user has all the data and can investigate areas that have been overlooked during the measurement stage in a second moment without having to return to the synchrotron. If the stability of the sample, the micro focused beam and the sample stage permit, the high photon flux density of modern synchrotrons allows to perform chemical imaging over a larger number of incident photon energies and thus to gain more detailed information on the spatial distribution of different chemical species.

RESEARCH DATA

Research Data (python scripts and raw data) associated with this article can be accessed at https://doi.org/10.25678/0002XK.

Declaration of Competing Interest

The authors declare that they have no known competing financial interests or personal relationships that could have appeared to influence the work reported in this paper.

ACKNOWLEDGEMENTS

We thank Silvan Wick and Numa Pfenninger (Eawag) for support with laboratory experiments and analyses, and Jonas Wielinski (Eawag) for the statistical tests performed on the chemical imaging data from Diamond. The Diamond Light Source (DLS; Didcot, UK) is acknowledged for the provision of beamtime at beamline I18 (microspectroscopic analyses on soil thin sections), the Swiss Light Source (SLS;Villigen, PSI) for beamtime at the microXAS endstation (preliminary analyses on thin sections and tests on Tl species stability as a function of photon flux density), and the French National Synchrotron Soleil (Gif-sur-Yvette, France) for beamtime at the beamline SAMBA (collection of reference spectra at 20 K). The beamline scientists Tina Geraki (DLS), Dario Ferreira Sanchez (SLS) and Gautier Landrot (Soleil) are acknowledged for their assistance during data collection. The directorates of PSI and Eawag are acknowledged for funding the postdoctoral research project of Francesco Femi Marafatto.

APPENDIX A. SUPPLEMENTARY MATERIAL

Supplementary data to this article can be found online at https://doi.org/10.1016/j.gca.2021.03.011.

REFERENCES

Bargar J. R., Fuller C. C., Marcus M. A., Brearley A. J., De la Rosa M. P., Webb S. M. and Caldwell W. A. (2009) Structural characterization of terrestrial microbial Mn oxides from Pinal Creek, AZ. *Geochim. Cosmochim. Acta* **73**, 889–910.

Baruchel J., Bleuet P., Bravin A., Coan P., Lima E., Madsen A., Ludwig W., Pernot P. and Susini J. (2008) Advances in synchrotron hard X-ray based imaging. *C. R. Phys.* **9**(5-6), 624–641.

Belzile N. and Chen Y.-W. (2017) Thallium in the environment: A critical review focused on natural waters, soils, sediments and airborne particles. *Appl. Geochem.* **84**, 218–243.

Bidoglio G., Gibson P. N., Ogorman M. and Roberts K. J. (1993) X-ray-absorption spectroscopy investigation of surface redox transformations of thallium and chromium on colloidal mineral oxides. *Geochim. Cosmochim. Acta* **57**, 2389–2394.

Bodei S., Manceau A., Geoffroy N., Baronnet A. and Buatier M. (2007) Formation of todorokite from vernadite in Ni-rich hemipelagic sediments. *Geochim. Cosmochim. Acta* **71**, 5698–5716.

Cruz-Hernandez Y., Villalobos M., Marcus M. A., Pi-Puig T., Zanella R. and Martinez-Villegas N. (2019) Tl(I) sorption behavior on birnessite and its implications for mineral structural changes. *Geochim. Cosmochim. Acta* **248**, 356–369.

De Samber B., Evens R., De Schamphelaere K., Silversmit G., Masschaele B., Schoonjans T., Vekemans B., Janssen C. R., Van Hoorebeke L., Szalóki I., Vanhaecke F., Falkenberg G. and Vincze L. (2008) A combination of synchrotron and laboratory X-ray techniques for studying tissue-specific trace level metal distributions in Daphnia magna. *J. Anal. At. Spectrom.* **23**(6), 829.

Dutrizac J. E., Chen T. T. and Beauchemin S. (2005) The behaviour of thallium(III) during jarosite precipitation. *Hydrometallurgy* **79**(3-4), 138–153.

Fuller C. C. and Harvey J. W. (2000) Reactive uptake of trace metals in the hyporheic zone of a mining-contaminated stream, Pinal Creek, Arizona. *Environ. Sci. Technol.* **34**(7), 1150–1155.

Gołębiowska B., Pieczka A., Zubko M., Voegelin A., Göttlicher J. and Rzepa G. (2021) Thalliomelane, $TlMn^{4+}{}_{7.5}Cu^{2+}{}_{0.5}O^{16}$, a new member of the coronadite group from the preglacial oxidation zone at Zalas, southern Poland. *Am. Mineral.*. https://doi.org/10.2138/am-2021-7577, in press.

Gonçalves Ferreira P., de Ligny D., Lazzari O., Jean A., Cintora Gonzalez O. and Neuville D. R. (2013) Photoreduction of iron by a synchrotron X-ray beam in low iron content soda-lime silicate glasses. *Chem. Geol.* **346**, 106–112.

Grabolle M., Haumann M., Muller C., Liebisch P. and Dau H. (2006) Rapid loss of structural motifs in the manganese complex of oxygenic photosynthesis by X-ray irradiation at 10–300 K. *J. Biol. Chem.* **281**, 4580–4588.

Grangeon S., Lanson B. and Lanson M. (2014) Solid-state transformation of nanocrystalline phyllomanganate into

tectomanganate: influence of initial layer and interlayer structure. *Acta Crystallogr. B Struct. Sci. Cryst. Eng. Mater.* **70**, 828–838.

Grolimund D., Senn M., Trottmann M., Janousch M., Bonhoure I., Scheidegger A. M. and Marcus M. (2004) Shedding new light on historical metal samples using micro-focused synchrotron X-ray fluorescence and spectroscopy. *Spectrochim. Acta B.* **59**, 1627–1635.

Herrmann J., Voegelin A., Palatinus L., Mangold S. and Majzlan J. (2018) Secondary Fe-As-Tl mineralization in soils near Buus in the Swiss Jura Mountains. *Eur. J. Mineral.* **30**, 887–898.

Houba V. J. G., Temminghoff E. J. M., Gaikhorst G. A. and van Vark W. (2000) Soil analysis procedures using 0.01 M calcium chloride as extraction reagent. *Commun. Soil. Sci. Plan.* **31**, 1299–1396.

Jacobson A. R., McBride M. B., Baveye P. and Steenhuis T. S. (2005) Environmental factors determining the trace-level sorption of silver and thallium to soils. *Sci. Total. Environ.* **345**, 191–205.

Kim J. G., Dixon J. B., Chusuei C. C. and Deng Y. J. (2002) Oxidation of chromium(III) to (VI) by manganese oxides. *Soil Sci. Soc. Am. J.* **66**, 306–315.

Kirkbright G., Mayne P. and West T. (1972) Photo-oxidation of thallium(I) with the production of hydrogen peroxide. *J. Chem. Soc., Dalton Trans.*, 1918–1920.

Kretzschmar R., Mansfeldt T., Mandaliev P. N., Barmettler K., Marcus M. A. and Voegelin A. (2012) Speciation of Zn in blast furnace sludge from former sedimentation ponds using synchrotron X-ray diffraction, fluorescence, and absorption spectroscopy. *Environ. Sci. Technol.* **46**(22), 12381–12390.

Lombi E. and Susini J. (2009) Synchrotron-based techniques for plant and soil science: opportunities, challenges and future perspectives. *Plant Soil* **320**(1-2), 1–35.

Manceau A., Lanson B. and Drits V. A. (2002) Structure of heavy metal sorbed birnessite. Part III: Results from powder and polarized extended X-ray absorption fine structure spectroscopy. *Geochim. Cosmochim. Acta* **66**(15), 2639–2663.

Manceau A., Lanson M. and Geoffroy N. (2007) Natural speciation of Ni, Zn, Ba, and As in ferromanganese coatings on quartz using X-ray fluorescence, absorption, and diffraction. *Geochim. Cosmochim. Acta* **71**(1), 95–128.

Manceau A., Marcus M. A. and Grangeon S. (2012) Determination of Mn valence states in mixed-valent manganates by XANES spectroscopy. *Am. Mineral.* **97**(5-6), 816–827.

Manceau A., Marcus M. A., Tamura N., Proux O., Geoffroy N. and Lanson B. (2004) Natural speciation of Zn at the micrometer scale in a clayey soil using X-ray fluorescence, absorption, and diffraction. *Geochim. Cosmochim. Acta* **68**, 2467–2483.

Marcus M. A. (2010) X-ray photon-in/photon-out methods for chemical imaging. *Trac-Trend. Anal. Chem.* **29**, 508–517.

Mosselmans J. F. W., Quinn P. D., Dent A. J., Cavill S. A., Moreno S. D., Peach A., Leicester P. J., Keylock S. J., Gregory S. R., Atkinson K. D. and Rosell J. R. (2009) I18–the microfocus spectroscopy beamline at the Diamond Light Source. *J. Synchrotron Radiat.* **16**(6), 818–824.

Nielsen S. G., Wasylenki L. E., Rehkamper M., Peacock C. L., Xue Z. C. and Moon E. M. (2013) Towards an understanding of thallium isotope fractionation during adsorption to manganese oxides. *Geochim. Cosmochim. Acta* **117**, 252–265.

Parise J. B. and Brown G. E. (2006) New opportunities at emerging facilities. *Elements* **2**(1), 37–42.

Peacock C. L. and Moon E. M. (2012) Oxidative scavenging of thallium by birnessite: Explanation for thallium enrichment and stable isotope fractionation in marine ferromanganese precipitates. *Geochim. Cosmochim. Acta* **84**, 297–313.

Pena J., Bargar J. R. and Sposito G. (2015) Copper sorption by the edge surfaces of synthetic birnessite nanoparticles. *Chem. Geol.* **396**, 196–207.

Peter A. L. J. and Viraraghavan T. (2005) Thallium: a review of public health and environmental concerns. *Environ. Int.* **31**(4), 493–501.

Post J. E. (1999) Manganese oxide minerals: crystal structures and economic and environmental significance. *Proc. Natl. Acad. Sci. USA* **96**, 3447–3454.

Ravel B. and Newville M. (2005) ATHENA, ARTEMIS, HEPHAESTUS: data analysis for X-ray absorption spectroscopy using IFEFFIT. *J. Synchrotron Radiat.* **12**(4), 537–541.

Remucal C. K. and Ginder-Vogel M. (2014) A critical review of the reactivity of manganese oxides with organic contaminants. *Environ. Sci. Process. Impacts.* **16**, 1247–1266.

Simanova A. A. and Pena J. (2015) Time-Resolved Investigation of Cobalt Oxidation by Mn(III)-Rich delta-MnO_2 Using Quick X-ray Absorption Spectroscopy. *Environ. Sci. Technol.* **49**, 10867–10876.

Solé V. A., Papillon E., Cotte M., Walter P. h. and Susini J. (2007) A multiplatform code for the analysis of energy-dispersive X-ray fluorescence spectra. *Spectrochim. Acta, Part B* **62**(1), 63–68.

Sposito G. (2008) *The chemistry of soils*, 2nd ed. Oxford University Press, Oxford.

Tebo B. M., Bargar J. R., Clement B. G., Dick G. J., Murray K. J., Parker D., Verity R. and Webb S. M. (2004) Biogenic manganese oxides: Properties and mechanisms of formation. *Annu. Rev. Earth Pl. Sc.* **32**, 287–328.

Tebo, B.M., Clement, B.G., Dick, G.J., 2007. Biotransformations of Manganese. In: Hurst, C.J., Crawford, R.L., Garland, J.L., Lipson, D.A., Mills, A.L., Stetzenbach, L.D. (Eds.), Manual of Environmental Microbiology, 3rd ed., pp. 1223-1238.

Teng T.-y. and Moffat K. (2000) Primary radiation damage of protein crystals by an intense synchrotron X-ray beam. *J. Synchrotron Radiat.* **7**(5), 313–317.

Toner B., Manceau A., Webb S. M. and Sposito G. (2006) Zinc sorption to biogenic hexagonal-birnessite particles within a hydrated bacterial biofilm. *Geochim. Cosmochim. Acta* **70**, 27–43.

Van Rossum, G. and Drake Jr, F.L. (1995) Python tutorial. Centrum voor Wiskunde en Informatica Amsterdam.

Vanek A., Chrastny V., Komarek M., Galuskova I., Drahota P., Grygar T., Tejnecky V. and Drabek O. (2010) Thallium dynamics in contrasting light sandy soils–soil vulnerability assessment to anthropogenic contamination. *J. Hazard. Mater.* **173**, 717–723.

Vaněk A., Chrastný V., Mihaljevič M., Drahota P., Grygar T. and Komárek M. (2009) Lithogenic thallium behavior in soils with different land use. *J. Geochem. Explor.* **102**, 7–12.

Vaněk A., Holubík O., Oborná V., Mihaljevič M., Trubač J., Ettler V., Pavlů L., Vokurková P., Penížek V., Zádorová T. and Voegelin A. (2019) Thallium stable isotope fractionation in white mustard: Implications for metal transfers and incorporation in plants. *J. Hazard. Mater.* **369**, 521–527.

Vanek A., Komarek M., Vokurkova P., Mihaljevic M., Sebek O., Panuskova G., Chrastny V. and Drabek O. (2011) Effect of illite and birnessite on thallium retention and bioavailability in contaminated soils. *J. Hazard. Mater.* **191**, 170–176.

Vaněk A., Voegelin A., Mihaljevič M., Ettler V., Trubač J., Drahota P., Vaňková M., Oborná V., Vejvodová K., Penížek V., Pavlů L., Drábek O., Vokurková P., Zádorová T. and Holubík O. (2020) Thallium stable isotope ratios in naturally Tl-rich soils. *Geoderma* **364**, 114183.

Villalobos M., Bargar J. and Sposito G. (2005) Mechanisms of Pb (II) sorption on a biogenic manganese oxide. *Environ. Sci. Technol.* **39**(2), 569–576.

Please cite this article in press as: Marafatto F. F., et al. Thallium sorption by soil manganese oxides: Insights from synchrotron X-ray micro-analyses on a naturally thallium-rich soil. *Geochim. Cosmochim. Acta* (2021), https://doi.org/10.1016/j.gca.2021.03.011

Voegelin A., Pfenninger N., Petrikis J., Majzlan J., Plötze M., Senn A.-C., Mangold S., Steininger R. and Göttlicher J. (2015) Thallium speciation and extractability in a thallium- and arsenic-rich soil developed from mineralized carbonate rock. *Environ. Sci. Technol.* **49**(9), 5390–5398.

Webb S. M., Tebo B. M. and Bargat J. R. (2005) Structural characterization of biogenic Mn oxides produced in seawater by the marine bacillus sp strain SG-1. *Am. Mineral.* **90**, 1342–1357.

Wick S., Baeyens B., Marques Fernandes M., Göttlicher J., Fischer M., Pfenninger N., Plötze M. and Voegelin A. (2020) Thallium sorption and speciation in soils: Role of micaceous clay minerals and manganese oxides. *Geochim. Cosmochim. Acta* **288**, 83–100.

Wick S., Baeyens B., Marques Fernandes M. and Voegelin A. (2018) Thallium adsorption onto illite. *Environ. Sci. Technol.* **52** (2), 571–580.

Wick S., Peña J. and Voegelin A. (2019) Thallium sorption onto manganese oxides. *Environ. Sci. Technol.* **53**(22), 13168–13178.

Wielinski J., Marafatto F. F., Gogos A., Scheidegger A., Voegelin A., Müller C., Morgenroth E. and Kaegi R. (2019) Software for: Synchrotron hard X-ray chemical imaging of trace element speciation in heterogeneous samples: Development of criteria for uncertainty analysis. *Eawag: Swiss Federal Institute Aquatic Science Technology*.

Wielinski J., Marafatto F. F., Gogos A., Scheidegger A., Voegelin A., Müller C. R., Morgenroth E. and Kaegi R. (2020) Synchrotron hard X-ray chemical imaging of trace element speciation in heterogeneous samples: development of criteria for uncertainty analysis. *J. Anal. Atom. Spectrom.* **35**(3), 567–579.

Associate editor: Georges Calas